

RESEARCH ARTICLE

10.1002/2015JD023364

Key Points:

- Climate feedback parameters obtained from idealized experiments do poorly at explaining twentieth century temperature change in CM3
- A Time-varying climate feedback parameter results in an incompatibility between radiative forcing techniques
- Regional climate feedback parameters and energy transport vary greatly between aerosol and greenhouse gas scenarios

Correspondence to:

D. Paynter,
David.Paynter@Noaa.gov

Citation:

Paynter, D., and T. L. Frölicher (2015), Sensitivity of radiative forcing, ocean heat uptake, and climate feedback to changes in anthropogenic greenhouse gases and aerosols, *J. Geophys. Res. Atmos.*, 120, doi:10.1002/2015JD023364.

Received 11 MAR 2015

Accepted 17 AUG 2015

Accepted article online 20 AUG 2015

Sensitivity of radiative forcing, ocean heat uptake, and climate feedback to changes in anthropogenic greenhouse gases and aerosols

D. Paynter¹ and T. L. Frölicher²

¹Geophysical Fluid Dynamics Laboratory, Princeton, New Jersey, USA, ²Environmental Physics, Institute of Biogeochemistry and Pollutant Dynamics, ETH Zürich, Zürich, Switzerland

Abstract We use both prescribed sea surface temperature and fully coupled versions of the Geophysical Fluid Dynamics Laboratory coupled climate model (CM3) to analyze the sensitivity of radiative forcing, ocean heat uptake, and climate feedback to changes in anthropogenic greenhouse gases and aerosols considered separately over the 1870 to 2005 period. The global anthropogenic aerosol climate feedback parameter ($-\alpha$) of $-1.13 \pm 0.33 \text{ Wm}^{-2} \text{ K}^{-1}$ is indistinguishable from the greenhouse gas $-\alpha$ of $-1.28 \pm 0.23 \text{ Wm}^{-2} \text{ K}^{-1}$. However, this greenhouse gas climate feedback parameter is about 50% larger than that obtained for CM3 from a widely used linear extrapolation method of regressing Earth's top of atmosphere imbalance against surface air temperature change in idealized CO_2 radiative forcing experiments. This implies that the global mean surface temperature change due to forcing over the 1870–2005 period is 50% smaller than that predicted using the climate feedback parameter obtained from idealized experiments. This difference results from time dependence in α , which makes the radiative forcing obtained by the fixed sea surface temperature method incompatible with that obtained by the linear extrapolation method fitted over the first 150 years after CO_2 is quadrupled. On a regional scale, α varies greatly between the greenhouse gas and aerosol case. This suggests that the relationship between transient and equilibrium climate sensitivities obtained from idealized CO_2 simulations, using techniques such as regional feedback analysis and heat uptake efficacy, may not hold for other forcing scenarios.

1. Introduction

For the Earth to be in radiative equilibrium, the incoming solar radiation must be balanced by the sum of the outgoing reflected solar radiation and emitted longwave radiation, resulting in a top of atmosphere imbalance of zero. After a radiative forcing (F) is applied, the change in top of atmosphere radiative imbalance (N) represents how far from equilibrium the planet is, whereas the difference between F and N indicates the radiation lost to space during the progress toward equilibrium. This progression toward equilibrium can result from changes in numerous properties of the climate system (cloud albedo, atmospheric temperature, water vapor, surface albedo, etc.). Following the notation of Gregory *et al.* [2004], this can be written as

$$N - F = -\alpha T, \quad (1)$$

where F is the global mean radiative forcing change since preindustrial (in units of Wm^{-2}), T is the global mean surface air temperature (K) change, N is the change in global mean top of the atmosphere imbalance (Wm^{-2}), and $-\alpha$ ($\text{Wm}^{-2} \text{ K}^{-1}$) is the climate feedback parameter. The climate feedback parameter ($-\alpha$) relates changes in any variables that affect the left-hand side of equation (1) to the change in global mean surface air temperature. It is generally assumed that changes in $N-F$ scale approximately linearly with surface air temperature change [e.g., Murphy, 1995; Crook *et al.*, 2011; Gregory *et al.*, 2004; Gregory and Webb, 2008; Williams *et al.*, 2008], and thus, α is approximately constant. Gregory *et al.* [2004] therefore proposed a “linear extrapolation method,” whereby a linear extrapolation of N against T , performed on a model held under constant F , allows α to be obtained from fully coupled general circulation model (GCM) runs before the model reaches equilibrium. Andrews *et al.* [2012], for example, estimated α using the first 150 years after a quadrupling of CO_2 using a number of coupled climate models that contribute to the fifth Coupled Model Intercomparison Project. This is notably less time than a fully coupled model takes to reach equilibrium (several thousand years [Li *et al.*, 2012]).

The assumption of a constant α has also been made in several recent studies that use a mixture of model and observational data to produce best estimates of F , N , and T for the present-day climate [e.g., *Otto et al.*, 2013; *Lewis and Curry*, 2014]. These values are used to calculate the equilibrium climate sensitivity (ECS), which is the equilibrium temperature reached in response to present-day radiative forcing if that forcing was the same strength as that brought about by a doubling of CO_2 . This can be written as

$$\text{ECS} = \frac{F_{2\times\text{CO}_2}}{F - N} T = \frac{F_{2\times\text{CO}_2}}{\alpha}, \quad (2)$$

where $F_{2\times\text{CO}_2}$ is the radiative forcing due to a doubling of CO_2 . By definition calculating ECS using singular values of F , N , and T assumes a constant α to equilibrium.

However, some recent studies suggest that α may change depending upon the state of the climate system as it responds to a radiative forcing [e.g., *Senior and Mitchell*, 2000; *Armour et al.*, 2013; *Feldl and Roe*, 2013]. Others propose that a constant α is only possible if adjustments for the spatial patterns of radiative forcing [*Hansen*, 2005] or ocean heat uptake [*Winton et al.*, 2010; *Rose et al.*, 2014; *Frölicher et al.*, 2014] are taken into account. This raises the question of whether α obtained using linear extrapolation, as well as other methods applied to idealized experiments, can provide any meaningful information about the α of CM3 when forced over the 1870–2005 historical period.

We investigate this question by performing a detailed global and regional analysis of the changes in the energy budget of CM3 over the 1870–2005 period for two individual forcing scenarios of anthropogenic aerosols (AERs) only and well-mixed greenhouse gases (GHGs) plus ozone only. In section 3.1 we calculate the radiative forcing and changes in surface air temperature and ocean heat content for these scenarios. These values are used to obtain a value of α that satisfies both the changes in energy budget and α being constant over the whole 1870–2005 period. We call this method of estimating α the Integrated Energy (IE) method, which is detailed in section 2. This method is similar to those which have been applied to construct a global energy budget in response to climate change, using observations or models [e.g., *Murphy et al.*, 2009; *Church et al.*, 2011; *Kummer and Dessler*, 2014]. In sections 3.2 and 3.3, we investigate a CM3 experiment in which CO_2 has been instantaneously quadrupled to provide a direct comparison between the IE and linear extrapolation methods.

In sections 3.4 and 3.5 we investigate the regional energy budget response of CM3 and assess if the concept of regional climate feedback [*Armour et al.*, 2013] is useful for understanding the climate responses. In section 3.6 we perform a similar analysis but looking at ocean heat uptake efficacy [*Winton et al.*, 2010, 2013; *Frölicher et al.*, 2014]. Finally, in section 3.7, we compare our results for the Transient Climate Response (TCR) to aerosols to those published in *Shindell* [2014].

2. Methods

2.1. The GFDL CM3 Model

The coupled climate model (CM3) of the Geophysical Fluid Dynamics Laboratory (GFDL) is a global model that includes aerosol-cloud interactions [*Donner et al.*, 2011]. The atmospheric model has 48 layers in the vertical, with enhanced vertical resolution in the stratosphere compared to earlier model versions such as CM2.1, and an approximate horizontal resolution of 200 km. The aerosol and ozone concentrations are calculated online in the model after specifying the emissions. The indirect effect of aerosols in the atmosphere is brought about by interactions between aerosol and liquid water clouds only [*Ming et al.*, 2006]. Although the emphasis in our paper is on the model response to forcing, rather than the realism of the forcing fields, we stress that there is still substantial uncertainty as to the true value of twentieth century aerosol radiative forcing, especially relating to its indirect effects upon clouds [e.g., *Boucher et al.*, 2013]. The comparatively large aerosol forcing of CM3 over the twentieth century has been noted by others [*Golaz et al.*, 2013; *Levy et al.*, 2013]. A detailed description of the atmospheric components of the model is given by *Donner et al.* [2011], while *Griffies et al.* [2011] provide a description of the ocean model, as well as the model in the coupled state.

2.2. Estimating Radiative Forcing and Top of the Atmosphere Imbalance

We apply the prescribed sea surface temperature (PSST) method to estimate the radiative forcing (F_{PSST} or F in equation (1)) [*Hansen*, 2002; *Shine*, 2003; *Andrews*, 2014]. The obtained radiative forcing is often

called effective radiative forcing [Myhre *et al.*, 2013] as it takes into account both tropospheric and stratospheric adjustments in response to a forcing agent that do not arise from sea surface temperature (SST) and sea ice changes. This method has been shown to produce reasonably accurate radiative forcing estimates [Hansen, 2005; Andrews, 2009]. We call N_{PSST} the difference between the top of atmosphere (TOA) imbalance from a simulation forced with 1870 to 2005 time series of both monthly varying prescribed SSTs from the Hadley Centre Sea Ice and Sea Surface Temperature data set (HADISST1) [Rayner *et al.*, 2003] and radiative forcing agents, compared to a simulation with the same monthly varying prescribed HADISST1 1870 to 2005 SSTs, but with radiative forcing agents set to preindustrial 1860 levels (note that our model integrations begin in 1870, but the control state used is year 1860).

To obtain an estimate of radiative forcing (F_{PSST}) we apply a small correction to N_{PSST} to account for the near-surface air temperature change (T_{PSST}) that occurs in the PSST case due to the land surface temperature not being fixed, such that

$$F_{\text{PSST}} = N_{\text{PSST}} + \alpha T_{\text{PSST}}. \quad (3)$$

F_{PSST} is an estimate of the TOA imbalance when there is no surface warming. Hence, this adjustment to N_{PSST} is required so that F , T , and N in equation (1) all represent changes from zero surface warming.

The benefit of the PSST method is that it allows a time series of radiative forcing to be obtained from 1870 to 2005. One caveat is that the PSST method assumes the same SSTs, regardless of forcing agent, and also uses different SSTs than those of the coupled model. Thus, we assume that these variations in the base state will not significantly alter the forcing between the coupled and fixed SST runs.

The TOA imbalance (N_{VSST} or N in equation (1)) is calculated from the difference between a fully coupled simulation run with a 1870 to 2005 time series of radiative forcing agents and a coupled control simulation with radiative forcing agents set to preindustrial 1860 levels. We call these variable SST (VSST) runs.

Substituting equation (3) into equation (1) (assuming $T = T_{\text{VSST}}$ and $N = N_{\text{VSST}}$ in equation (1)) allows α to be estimated from the VSST and PSST runs,

$$N_{\text{VSST}} - N_{\text{PSST}} = -\alpha(T_{\text{VSST}} - T_{\text{PSST}}). \quad (4)$$

It follows that α is derived for a change of T from T_{PSST} to T_{VSST} . We assume that this α can also be used in equation (3) to make the small correction (~5%) to N_{PSST} required to obtain F_{PSST} and therefore is also valid to be used in equation (1). However, the different warming patterns in the PSST and VSST cases mean that the actual α required for the correction in equation (3) may be different.

2.3. Estimating the Climate Feedback Parameter With the IE Method

The IE method takes equation (4), which contains global mean quantities and integrates it over time and surface area, so that the left-hand side represents the magnitude of total energy lost to space (in units of joules) by the planet between times t_1 and t_2 . The right-hand side is equal to α multiplied by the global mean surface air temperature change, integrated between times t_1 and t_2 and intergrated over surface area between a_1 and a_2 . This can be written as

$$\int_{t_1}^{t_2} \int_{a_1}^{a_2} N_{\text{VSST}} da dt - \int_{t_1}^{t_2} \int_{a_1}^{a_2} N_{\text{PSST}} da dt = - \int_{t_1}^{t_2} \int_{a_1}^{a_2} \alpha (T_{\text{VSST}} - T_{\text{PSST}}) da dt, \quad (5)$$

where a is surface area (m^2), t is time (s), and all others terms are as described for equation (4). To be consistent with our definitions in equations 1–4, N and T in equation (5) are the global means. However, equation (5) would produce identical answers if these represented values at specific grid points.

For ease of notation, we define the integrals in equation (5) over time and surface area of N_{VSST} , N_{PSST} , T_{VSST} , and T_{PSST} as $N_{\text{I,VSST}}$, $N_{\text{I,PSST}}$, $T_{\text{I,VSST}}$, and $T_{\text{I,PSST}}$, respectively (e.g., $N_{\text{I,VSST}}$ is the first term on the left side of equation (5)). Accordingly, $N_{\text{I,VSST}}$ represents the total energy stored by the Earth, which is almost identical to the change in ocean heat content (OHC), since most energy is stored by the oceans. $N_{\text{I,PSST}}$ represents the total energy that would be stored by the Earth if SSTs were fixed. Using this

notation, if α is considered to be constant, we can rearrange equation (5) to state that for the whole 1870–2005 period,

$$-\alpha = \frac{NI_{VSST} - NI_{PSST}}{TI_{VSST} - TI_{PSST}}. \quad (6)$$

Calculating the ratio of energy lost to space to surface air temperature change integrated over surface area and time can thus be seen as an alternative method for estimating α . The same ratio can be achieved using 1870–2005 time-averaged values of N_{PSST} , N_{VSST} , T_{VSST} , and T_{PSST} (noting that each value is already a global average).

We also make use of the large-scale regional energy budgets to estimate the regional climate feedback parameter $-\alpha_{\phi_1:\phi_2}$ for zonal mean regions constrained between latitudes ϕ_1 and ϕ_2 . If it is assumed that $\alpha_{\phi_1:\phi_2}$ is not a function of time, we can then write equation (6) as

$$-\alpha_{\phi_1:\phi_2} = \frac{NI_{VSST}(\phi_1:\phi_2) - NI_{PSST}(\phi_1:\phi_2)}{(TI_{VSST}(\phi_1:\phi_2) - TI_{PSST}(\phi_1:\phi_2))}, \quad (7)$$

where the notation $\phi_1:\phi_2$ represent the lower and upper limits of the latitudes over which the terms on the right-hand side are integrated.

2.4. Natural Variability and Error Analysis

All results, unless otherwise stated, are the average of three ensemble members of the specified forcing scenario. For these ensembles we estimate the magnitude of unforced variability by using an 800 year preindustrial 1860 control run of CM3. For each variable we randomly select two 136 year periods from the 800 year control run and subtract one from the other. We assume that one of these periods represents the control and the other the experiment. This operation is performed 30,000 times. The resulting distribution is then used to directly estimate the 95% confidence interval for each variable.

We assume that all changes in energy stored by the planet in response to the GHG or AER forcing scenarios go into OHC changes and hence neglect the minor changes in atmosphere, land, and ice heat storage. Additionally, CM3 does not perfectly conserve energy in the ocean or atmosphere. To close the global energy budget we scale the changes in the global values of both time-integrated surface heat flux (SHFI) and OHC (in the VSST cases) to equal NI. The sizes of these adjustments are comparatively small. For example, the range between NI, SHFI, and OHC is 4×10^{22} J and 3×10^{22} J in the GHG and AER VSST runs, respectively. This range is less than the unforced variability in NI, SHFI, and OHC, which for all three variables is $\pm 10 \times 10^{22}$ J.

3. Results

3.1. Radiative Forcing, Ocean Heat Uptake, and Global Climate Feedback Factor

Figure 1 shows the time-integrated TOA imbalance from the PSST run NI_{PSST} (Figures 1a and 1b), the ocean heat uptake NI_{VSST} (Figures 1c and 1d), and the difference between NI_{VSST} and NI_{PSST} (Figures 1e and 1f) in units of 10^{22} J for the GHG (Figures 1a, 1c, and 1e) and AER (Figures 1b, 1c, and 1f) scenarios over the 1870–2005 period. Table 1 can be used to convert energy (joules) values to average fluxes (Wm^{-2}) over the 136 year period (100×10^{22} J = 0.46 Wm^{-2}).

In both the GHG and AER scenarios, over the 1870–2005 period approximately 40% (i.e., 94/251 for GHG or 67/163 for AER) of the energy change is retained by the planet (Figure 1, middle row) and the other 60% is lost to space (Figure 1, bottom row). As detailed in section 2.3, the lost-to-space energy (Figure 1, bottom row) can be used to obtain an estimate of α over the 1870–2005 period. Feedback parameter α for the GHG case is $1.28 \text{ Wm}^{-2} \text{ K}^{-1}$ (i.e., $(251-94)/(0.59-0.03) = 280 \times 10^{22} \text{ JK}^{-1} = 1.28 \pm 0.23 \text{ Wm}^{-2} \text{ K}^{-1}$), which is slightly larger than α for the AER case ($1.13 \pm 0.33 \text{ Wm}^{-2} \text{ K}^{-1}$). The differences are not significant at the 95% confidence level. As noted in section 2, the NI_{PSST} value is not a true representation of the time-integrated radiative forcing, as it needs to be corrected for the change in land surface temperatures (equation (3)). This results in an estimate of FI_{PSST} for the GHG and AER cases of 260×10^{22} J and -173×10^{22} J, respectively.

Next, we investigate the time series of both flux and energy from the GHG and AER experiments in Figure 2. The time series of N_{PSST} (in Wm^{-2}) reveals that both the GHG (Figure 2a) and AER (Figure 2b) cases indicate a steady increase in the forcing magnitude during the first half of the twentieth century and that for both

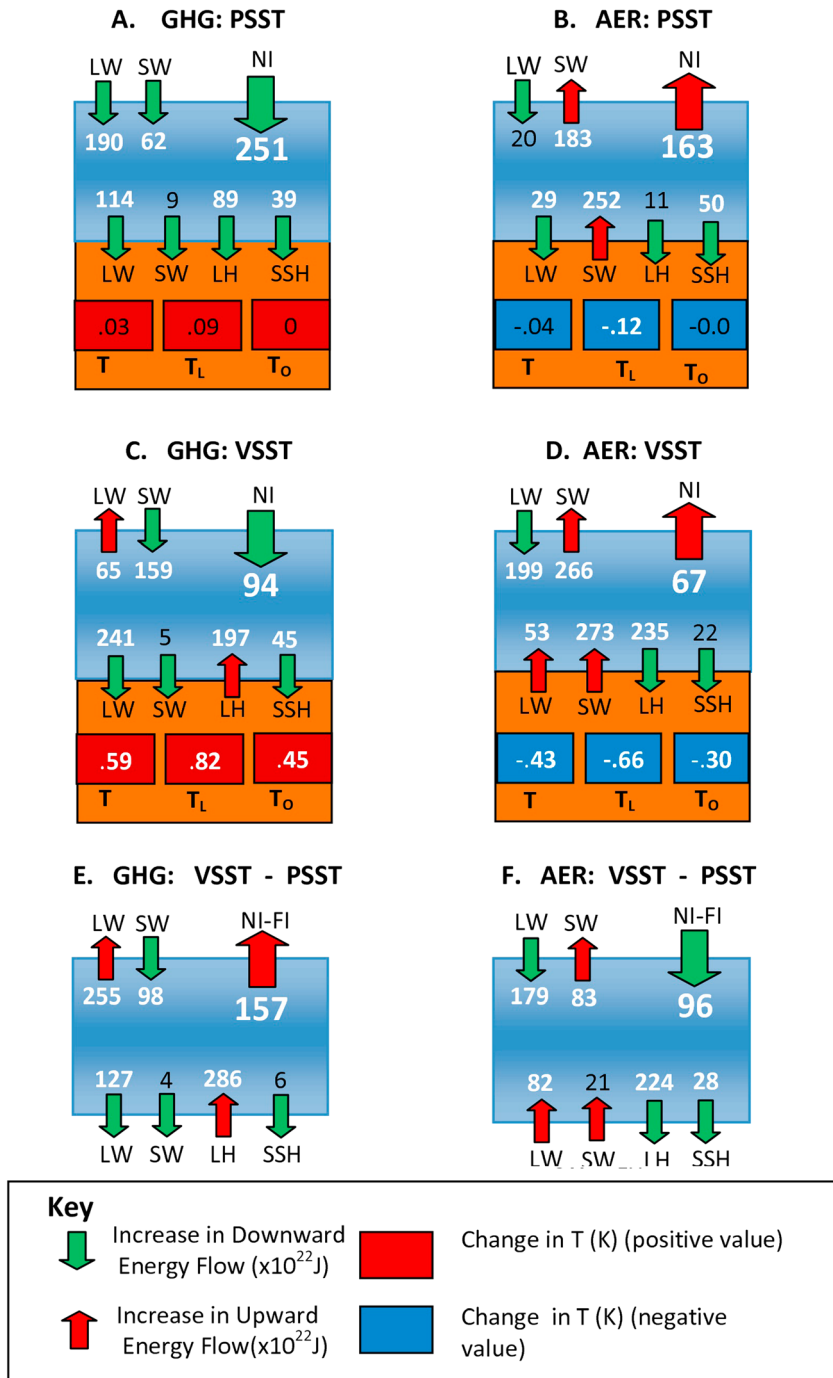


Figure 1. Simulated changes in key energy budgets terms over the 1870–2005 period for the (a, c, and e) GHG and (b, d, and f) AER cases. (Figures 1a and 1b) The changes in 10^{22} J over the 1870–2005 period relative to the 1860 climate estimated for various energy budget terms for the PSST runs. (Figures 1c and 1d) As above but for the VSST runs. (Figures 1e and 1f) The difference between the VSST and PSST runs. Temperature changes (T) are also given and represent the change in surface air temperature averaged over the whole 1870–2005 period compared to the 1860 climate. The bold white numbers are statistically significant at the 95% level, while the black nonbold values are not statistically significant. The arrow direction and color show whether the energy flow change is positive (green arrow and downward) or negative (red arrow and upward). Definitions of symbols: LW = net longwave energy (10^{22} J), SW = net shortwave energy (10^{22} J), LH = latent heat energy (10^{22} J), SSH = sensible heat energy (10^{22} J). Changes in average global surface air temperature (T), land surface air temperature L should be subscript, (T_L), and ocean surface air temperature (T_O) in units of kelvin are also shown. A blue box represents a decrease in T and a red box an increase.

Table 1. The Equivalent Values in Joules, Pettawatts, and Wm^{-2} Both Globally and for Different Latitude Bands^a

Latitude	90–60	60–30	30–0	Global
Joules(10^{22} J)	100	100	100	100
Average PW (10^{15} W) (136 years)	0.23	0.23	0.23	0.23
Average Wm^{-2} (136 years)	6.82	2.51	1.83	0.46
Percentage surface area	6.7	18.3	25	100
Surface area (10^{15} m ²)	0.03	0.09	0.13	0.51
Surface area land (%) SH, NH	38,52	6,48	22,27	28%

^aIn all cases the values are assumed for the 136 years of the historical run. The percentage surface area and total surface area are also given along with percentage area land cover.

the increase becomes more rapid in the second half. However, the rate of increase in the magnitude of aerosol forcing lessens after 1965. By year 2000 N_{PSST} is $3.2 Wm^{-2}$ and $-1.8 Wm^{-2}$ for GHG and AER, respectively. Applying the correction in equation (3) results in an estimated radiative forcing (F_{PSST}) for GHG of $3.3 Wm^{-2}$ and for AER of $-1.9 Wm^{-2}$.

A time series of α (Figure 2e) can also be estimated by rearranging equation (4) to calculate α from the 10 year running

average time series of N_{PSST} , N_{VSST} , T_{VSST} , and T_{PSST} . If the model unforced variability were zero and α constant, this would produce identical values to the IE method. However, as the individual ensemble members in Figure 2e show, for much of the twentieth century unforced variability presents an obstacle to calculating

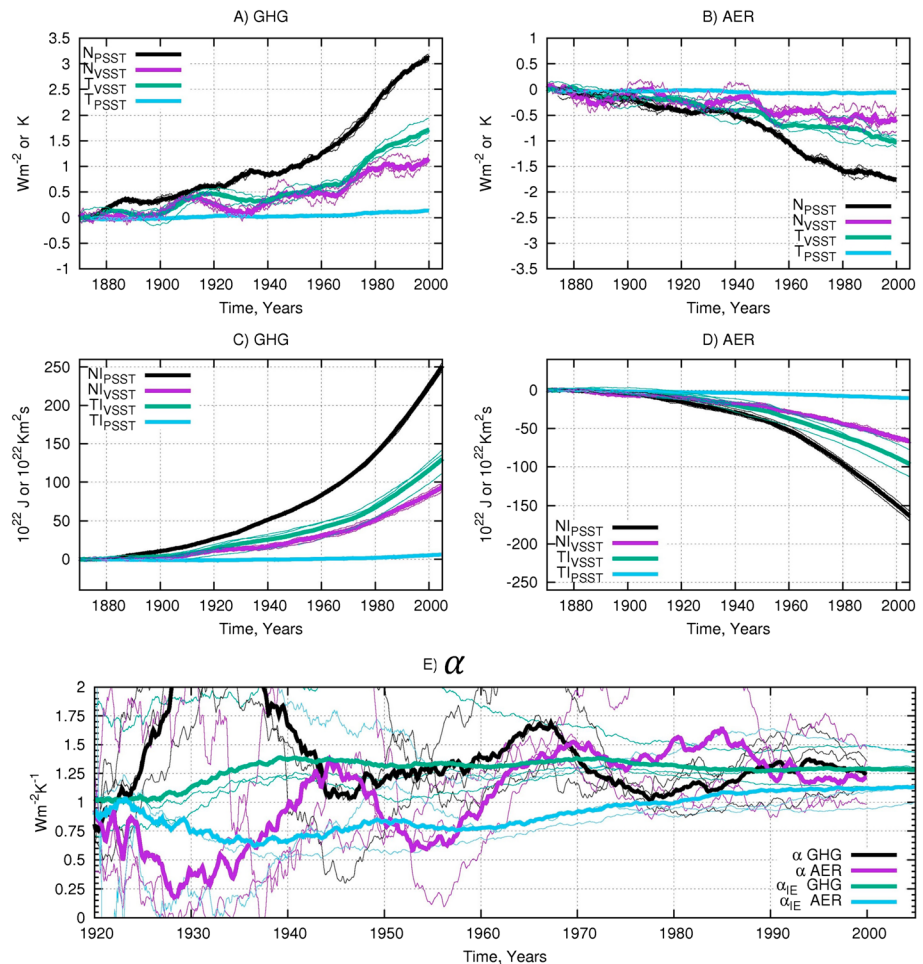


Figure 2. Time series of simulated changes in flux and energy from the GHG and AER experiments. (a) Ten-year running average of N_{PSST} (Wm^{-2}), N_{VSST} (Wm^{-2}), T_{PSST} (K), and T_{VSST} (K) over the 1870–2005 period for the GHG forcing scenario. (b) Same as Figure 2a but for the AER scenario. (c) The integration of the curves in Figure 2a over time and space to obtain N_{IPSSST} (10^{22} J), N_{IVSSST} (10^{22} J), T_{IPSSST} (10^{22} Km^2s), and T_{IVSSST} (10^{22} Km^2s). (d) Same as Figure 2c but for the AER scenario. (e) Feedback parameter α ($Wm^{-2} K^{-1}$) calculated between 1920 and 2000 for the GHG and AER scenarios using equation (4) and values given in Figures 2a and 2b, respectively. Feedback parameter α_{IE} ($Wm^{-2} K^{-1}$) is shown between 1920 and 2005 for the GHG and AER scenarios using equation (6) and values given in Figures 2c and 2d, respectively. Note for the IE method the integration begins in 1870. For all plots the individual ensemble members are shown (thin lines) and as well as the ensemble mean (thick lines).

α to a sufficiently useful precision. This is also why the years prior to 1920 are not shown. After 1980, when the values of T_{VSST} and N_{VSST} are greater, the values of α are more stable, but there is still a spread of $\sim 0.5 \text{ Wm}^{-2} \text{ K}^{-1}$ across the six ensemble members.

Focusing on the energy variables again, the evolution of N_{PSST} , N_{VSST} , T_{VSST} , and T_{PSST} over the 1870–2005 period is shown for the GHG (Figure 2c) and AER (Figure 2d) cases. These values can then be used in equation (6) to calculate a time series of α estimated by the IE method (denoted α_{IE} in Figure 2e) over the 1920–2005 period. The IE technique, due to its integrated nature, results in more stable α values than those calculated using the 10 year averages of N_{PSST} , T_{VSST} , N_{VSST} , and T_{PSST} . However, the individual ensemble members (thin lines) show that, even by year 2005, long-term unforced variability, mainly in T_{VSST} , result in an equally large spread in α_{IE} and α .

3.2. Reconciling Different Estimates of the Global Climate Feedback Parameter for GFDL CM3

The values of α for the AER and GHG cases of CM3 over the 1870–2005 period, obtained using the IE method, are $\sim 50\%$ larger than those obtained by others for CM3 using the linear extrapolation method [Gregory *et al.*, 2004]. Kuhlbrodt and Gregory [2012], for example, estimate α to be $0.74 \text{ Wm}^{-2} \text{ K}^{-1}$ using a simulation in which CO_2 is increased by 1%/yr until doubling. Using the same technique, but with a 150 year simulation where CO_2 is instantaneously quadrupled, Andrews *et al.* [2012] estimate α to be $0.75 \text{ Wm}^{-2} \text{ K}^{-1}$ and the forcing to be 6.0 Wm^{-2} . The forcing of 6.0 Wm^{-2} estimated by Andrews *et al.* [2012] is considerably less than 7.6 Wm^{-2} , which is the instantaneous forcing at the tropopause calculated for CM3 using the GFDL stand-alone radiation code [Schwarzkopf and Ramaswamy, 1999].

This difference in radiative forcing might be explained by fast adjustments to the forcing, in both the stratosphere and troposphere, not caused by warming SSTs. However, the PSST method used to calculate N_{PSST} for the GHG and AER cases in the previous section should account for stratosphere and troposphere adjustments. We thus calculate F from the TOA imbalance of a 30 year 1860 PSST run, in which CO_2 is instantaneously quadrupled from 287 to 1148 ppmv. From this, a value of N_{PSST} of 7.0 Wm^{-2} is obtained for the first year after quadrupling the CO_2 . Over the 30 year run period this value increases slightly; the average N_{PSST} for years 20 to 30 is only marginally higher at 7.3 Wm^{-2} . To obtain an estimate of radiative forcing, this value has to be corrected for surface temperature rise in the PSST run (see equation (3)). Assuming an average N_{PSST} of 7.1 Wm^{-2} , α of $1.1 \text{ Wm}^{-2} \text{ K}^{-1}$ and T_{PSST} of 0.45 K in equation (3) gives a F_{PSST} of 7.6 Wm^{-2} . Thus, it appears that even once stratosphere and troposphere adjustments are taken into account, the PSST method results in an $\sim 25\%$ larger forcing than that obtained by Andrews *et al.* [2012] using the linear extrapolation method.

To estimate α for the quadrupling CO_2 case we make use of a 180 year VSST run of CM3, in which CO_2 is instantaneously quadrupled from 287 to 1148 ppmv at the beginning of the experiment (i.e., the same experiment as used by Andrews *et al.* [2012] but with 30 years of additional data). Here similar to calculating α in Figure 2e, we take the 10 year running averages of N_{VSST} and T_{VSST} and calculate α using equation (4) as a function of time, with an N_{PSST} that we assume to be fixed at 7.1 Wm^{-2} and T_{PSST} fixed at 0.5 K. Figure 3a (red line) shows that the value of α decreases from 1.6 to $1.2 \text{ Wm}^{-2} \text{ K}^{-1}$ during the first 30 years after quadrupling. This range is in good agreement with the values obtained for the GHG and AER experiments in section 3.1. Conversely, a lower value of α (around $1.00 \text{ Wm}^{-2} \text{ K}^{-1}$) seems to work better after year 100. However, this value is still larger than the $0.75 \text{ Wm}^{-2} \text{ K}^{-1}$ predicted by the linear extrapolation method.

In Figure 3b we demonstrate that surface air temperature change (T_{VSST}) is overpredicted using a rearranged equation (1) if an α value of $0.75 \text{ Wm}^{-2} \text{ K}^{-1}$, obtained from the linear extrapolation method, and a forcing of 7.6 Wm^{-2} , obtained from the PSST method, are used (Figure 3b, green line compared to black line which is T_{VSST}). Using a value of α of $1.10 \text{ Wm}^{-2} \text{ K}^{-1}$ (the average from the VSST quadrupling CO_2 run) with a forcing of 7.6 Wm^{-2} produces a much better agreement (Figure 3b, red line) but still overpredicts the temperature change during the first 50 years and underpredicts after year 100. This again confirms the need for a time-varying α as seen in Figure 3a when a forcing of 7.6 Wm^{-2} is used.

In Figure 3b we also plot the time series of T (blue line) predicted with equation (1) using an F of 6.0 Wm^{-2} and $\alpha = 0.75 \text{ Wm}^{-2} \text{ K}^{-1}$, both obtained using the linear extrapolation method. Apart from a small overestimation between years 20 and 50, this results in a similar estimate of the temperature change as assuming a F_{PSST}

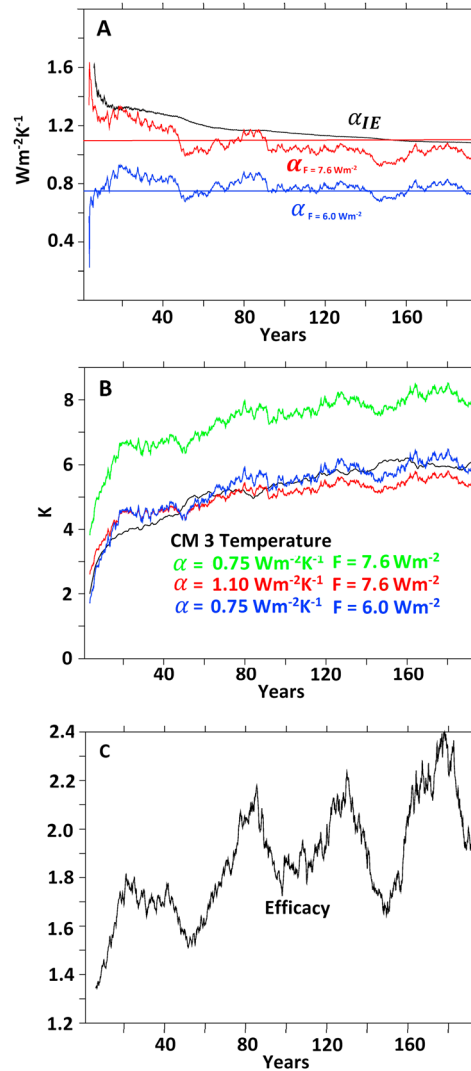


Figure 3. Feedback parameter α (the climate feedback parameter*⁻¹, $\text{Wm}^{-2}\text{K}^{-1}$) calculated as a function of time in the 180 years following an instantaneous quadrupling of CO_2 . In one case (red line) a constant N_{PSST} of 7.1 Wm^{-2} is used in equation (4), and in another (blue line) a constant F from the linear extrapolation method of 6.0 Wm^{-2} is used in equation (1). In both cases N_{VSST} and T_{VSST} values are taken from the VSST run. So to make the time dependence clearer, the accompanying straight lines show an $\alpha = 1.1 \text{ Wm}^{-2}\text{K}^{-1}$ (red) and $\alpha = 0.75 \text{ Wm}^{-2}\text{K}^{-1}$ (blue). Feedback parameter α_{IE} (black line) calculated using equation (6), using data from the instantaneous quadrupled CO_2 PSST and VSST runs (Figure 3b). The change in global mean surface air temperature (black line) after a quadrupling of CO_2 obtained from the CM3 VSST run and various estimates obtained using a rearranged equation (1) (colored lines). The green line is calculated with an α of $0.75 \text{ Wm}^{-2}\text{K}^{-1}$ and F of 7.6 Wm^{-2} . The red line is calculated with an α of $1.10 \text{ Wm}^{-2}\text{K}^{-1}$ and F of 7.6 Wm^{-2} . The blue is calculated with an α of $0.75 \text{ Wm}^{-2}\text{K}^{-1}$ and F of 6.0 Wm^{-2} . For all colored lines α and F are held constant, and the value of N is taken from the VSST run. (Figure 3c) The heat uptake efficacy (ϵ_N) calculated for the instantaneous quadrupling of CO_2 experiment by rearranging equation (8). F is assumed to be 7.6 Wm^{-2} , and $\alpha(t_{\text{eq}})$ is assumed to be $0.75 \text{ Wm}^{-2}\text{K}^{-1}$. Feedback parameter $\alpha(t_{\text{eq}})$ and F are held constant, and the value of N is taken from the VSST run. All panels show 10 year running averages.

of 7.6 Wm^{-2} and α of $1.1 \text{ Wm}^{-2}\text{K}^{-1}$. This result is confirmed in Figure 2a, where the time evolution of α is plotted assuming linear extrapolation F of 6.0 Wm^{-2} (blue line) and shows that a value of $\sim 0.75 \text{ Wm}^{-2}\text{K}^{-1}$ works well over years 50–180.

This result is somewhat consistent with findings by Williams *et al.* [2008], which show that the time dependence of α could result from a misdiagnosis of the radiative forcing. The authors suggest that the main reason for a time-varying α is the use of methods, when obtaining radiative forcing (e.g., fixed SST, instantaneous, and stratospherically adjusted), that do not implicitly take into account the fast adjustments to forcing observed in the fully coupled model.

Therefore, after a quadrupling of CO_2 using both F and constant α from the linear extrapolation method perform as well as, if not slightly better after year 50, than using F from the PSST run with a constant α value. However, the key result here is that for CM3 it is important not to use the forcing derived from one method with α derived from another or vice versa.

In the Introduction the question was asked as to whether the α obtained for CM3 from the linear extrapolation method can be of practical use for predicting the behavior of CM3 when forced with AER and GHG scenarios over the 1870–2005 period. The larger α calculated for both the AER and GHG scenarios suggest that the model is far less sensitive during the historical period. However, it is apparent that some of this difference arises from the way radiative forcing is defined. If the PSST definition of radiative forcing is assumed in the idealized quadrupling of CO_2 experiments it is possible to obtain an α much nearer that seen in the AER or GHG experiments. However, this also resulted in a time dependence in α .

Thus, there is a problem in translating α from the idealized experiment to the AER and GHG scenarios regardless of

the method used for estimating radiative forcing and α . If one wants to apply the smaller α from the linear extrapolation method to the GHG and AER cases, there is a need to adjust the radiative forcing over the 1870–2005 period. However, there remains the problem of working out how much the forcing should be adjusted by. On the other hand, if one wants to use the PSST forcing and the α from the quadrupling CO₂ experiment, the problem is then determining at which point in time the α from the quadrupling CO₂ experiment is applicable to GHG and AER experiments.

For the remainder of this paper we use the framework of looking at the adjustments in α necessary if F_{PSST} or F_{PSST} are used. This is because any adjustments which occur between the PSST forcing and linear extrapolation forcing are by definition due to the SST changes, even if the adjustment happens on a fast time scale and may be convenient to include in the forcing.

3.3. The Implications of a Time-Dependent α

A time dependence in α means that it is important not to interpret α calculated using 10 year averages of fluxes and temperatures as the actual feedback of the model at any particular point in time. The changes in flux and temperature are always relative to the 1860 control. Therefore, α calculated for a particular year is the average feedback of the model weighted by temperature change since the radiative forcing was applied.

This time dependence also implies that ECS calculated using equation (2) from present-day values of F , N , and T should be adjusted to account for the smaller α values in equilibrium. As was concluded in the last section it is not apparent how applicable the time dependence seen in idealized experiments is to historical ones. However, an idea of the possible size of adjustment in CM3 can be obtained by assuming that the α of $1.3 \text{ Wm}^{-2} \text{ K}^{-1}$ from the GHG scenario represents a present-day value and α of $1.0 \text{ Wm}^{-2} \text{ K}^{-1}$ from year 150–180 after a quadrupling of CO₂ represents an equilibrium value. This means that the uncorrected ECS values calculated in year 2000 using equation (2) for the GHG and AER cases, of 3.0 K and 3.3 K, respectively, would become 4.0 K and 4.3 K, respectively. If the real world also exhibited such time dependence the ECS value of 2.0 K from *Otto et al.* [2013] would become 2.6 K and that of *Lewis and Curry* [2014] of 1.6 K would become 2.1 K.

Another consequence of time dependence in α is that the IE method, which makes use of the PSST method to define F_I , will produce different values for α depending upon the time period it is applied to after the quadrupling of CO₂. Applied 0 to 5 years after the quadrupling we obtained a value of $1.55 \text{ Wm}^{-2} \text{ K}^{-1}$. This decreases to $1.42 \text{ Wm}^{-2} \text{ K}^{-1}$ for the time period 0 to 10 years and further decreases to $1.08 \text{ Wm}^{-2} \text{ K}^{-1}$ for the 0 to 200 year period. The time series is shown in Figure 3a.

Despite this, α calculated by the IE method (i.e., using equation (6)) provides a meaningful metric from which to evaluate the climate response to time-varying feedback. The benefit of using α calculated by the IE method rather than α calculated from short-term averages (i.e., 10 years) is that the former relates the total energy lost to space by the planet to the average surface air temperature change of the planet required to lose this energy. It can be easily shown that two worlds can end up in identical states of F , T , and N , but have had different average temperatures in reaching that state, depending upon when in time the feedback changed. Therefore, for a particular time period α calculated by the IE method captures the impact of time-varying α upon surface air temperature more effectively than α calculated by short-term averages at end of that time period.

3.4. Regional Energy Budget Response of CM3

Consistent with previous work [e.g., *Williams et al.*, 2008; *Winton et al.*, 2010, 2013; *Armour et al.*, 2013; *Frölicher et al.*, 2014; *Rose et al.*, 2014; *Andrews et al.*, 2015] we have shown that it is difficult to explain the global energy budget changes for CM3 using a simple global forcing and feedback model as defined by equation (1). In this section we attempt to see if it is possible to better understand the changes in the GHG and AER cases if the world is broken down into six large-scale regions, each of 30° latitude. Our key aim is to understand how the forced energy gets stored, lost to space, or transported across the regions. We also estimate α by the IE method for each of these regions (α_i , where i refers to the region in question).

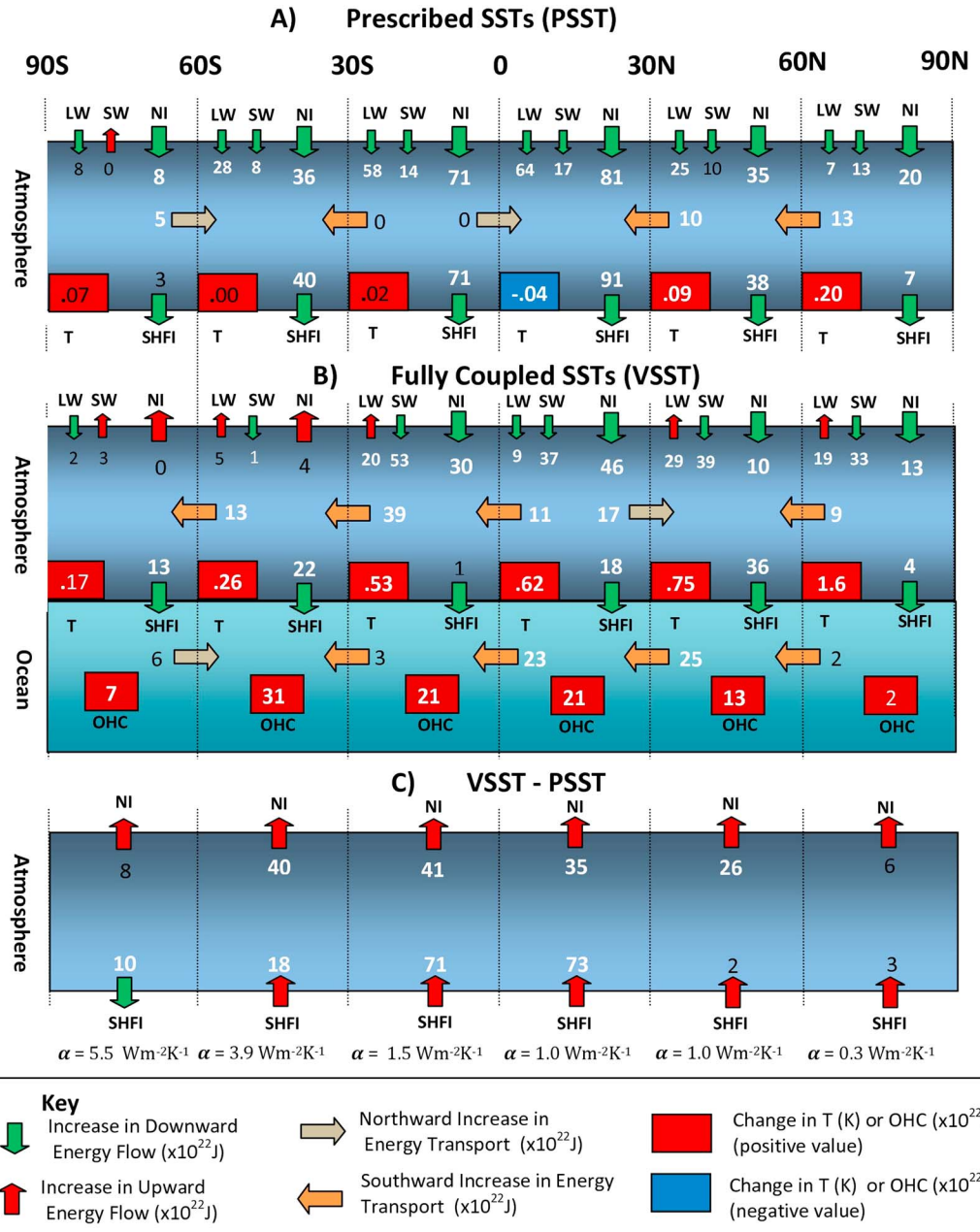


Figure 4. Energy budget changes for the (a) PSST and (b) VSST cases in response to GHG forcing over the 1870–2005 period. (Figure 4a) The changes in key energy budget terms over the 1870–2005 period for the GHG PSST experiment relative to the 1860 climate. Apart from mean 1870–2005 surface air temperature (K), all values are in units of $10^{22} J$. The symbol and sign conventions are as used in Figure 1. Additionally, the meridional atmospheric heat transport between the regions is shown. A light grey arrow represents northward transport and orange arrow southward transport. (Figure 4b) As above but for the VSST case. The changes in OHC and meridional oceanic heat transport between the regions are also shown. For OHC a red colored box represents an increase in OHC and a blue box a decrease. (Figure 4c) $SHFI_{VSST}$ minus $SHFI_{PSST}$ (bottom arrows) and NI_{VSST} minus NI_{PSST} (top arrows). Feedback parameter α_i ($Wm^{-2}K^{-1}$) is also shown for each region and are both calculated with the Integrated Energy method as detailed in equation (7).

3.4.1. GHG 1870–2005 Scenario

We start by looking at the GHG 1870–2005 scenario. Figure 4 shows the changes in energy budget at TOA (i.e., NI) and surface (i.e., SHFI) for each 30° region and has a similar layout to Figure 1 (except individual surface energy terms are now excluded to give a clearer schematic); the top plot (Figure 4a) shows the PSST runs and the middle plot (Figure 4b) the VSST runs. The atmospheric and oceanic heat transport

between regions is also shown (using arrows) along with regional ocean heat storage. The bottom plot (Figure 4c) shows the difference between the PSST and VSST cases for both SHFI and NI. The values of α_i (regional climate feedback parameters⁻¹) are also shown for each region (Figure 4, bottom).

Our analysis shows that the GHG large-scale regional energy budget can be characterized by the majority of the integrated forcing (Figure 4a) occurring in the tropics (30°S, 30°N) (60%, $71 + 81 = 152 \times 10^{22}$ J) but with most of the heat uptake (Figure 4b) occurring outside of this region (80%, $13 + 22 + 36 + 4 = 75 \times 10^{22}$ J). In the tropics, while a substantial amount of the energy forced into the system is lost to space ($41 + 35 = 76 \times 10^{22}$ J; Figure 4c), a large proportion ($39 + 17 = 56 \times 10^{22}$ J; Figure 4b) is also transported to the middle (30°S–60°S, 30°N–60°N) and high (60°S–90°S, 60°N–90°N) latitudes, with the majority of this energy transport occurring in the Southern Hemisphere (SH). Both Northern Hemisphere (NH) and SH tropics have similar integrated radiative forcings (81×10^{22} J versus 71×10^{22} J; Figure 4a), but the NH warms by ~ 0.1 K more than the SH. This, coupled with a greater energy transport out of the SH tropics, results in a smaller value of $\alpha_{0^\circ\text{N}-30^\circ\text{N}}$ for the NH ($1.0 \text{ Wm}^{-2} \text{ K}^{-1}$) than $\alpha_{0^\circ\text{S}-30^\circ\text{S}}$ for the SH ($1.5 \text{ Wm}^{-2} \text{ K}^{-1}$).

The atmospheric energy transported south of 30°S (39×10^{22} J; Figure 4b) is comparable to the local integrated radiative forcing south of 30°S (44×10^{22} J). Similarly, considerable energy is transported (26×10^{22} J; Figure 4b) into the NH midlatitudes from both the north and south. However, despite similar magnitudes of forcing, heat uptake, and energy transport in the two midlatitude regions, the SH midlatitudes warm far less than the NH ones (0.26 K in the SH versus 0.75 K in the NH; Figure 4b). Accordingly, $\alpha_{30^\circ\text{N}-60^\circ\text{N}}$ is much smaller ($1.0 \text{ Wm}^{-2} \text{ K}^{-1}$) than $\alpha_{30^\circ\text{S}-60^\circ\text{S}}$ ($3.9 \text{ Wm}^{-2} \text{ K}^{-1}$).

In the CM3 GHG case, energy transport by the ocean also plays a key role. GHG forcing results in a net southward heat transport at most latitudes (Figure 4b). At 30°N the changes in ocean and atmospheric heat transport are in opposite directions (Figure 4b). This implies that a substantial amount of the excess energy absorbed at middle and high northern latitudes is transported southward and stored in the tropical oceans. In contrast, the southern ocean in CM3 does not respond in this way, but instead, most of the energy is stored locally [Frölicher *et al.*, 2015]. Therefore, the majority of heat uptake in CM3 occurs in the NH, but the majority energy from this is stored in the SH.

The NH high latitudes exhibit some very interesting behaviors (Figures 4a–4c). Despite a high level of warming in the region, energy is mostly exported to south of 60°N. This results in the region having an extremely sensitive climate, with an $\alpha_{60^\circ\text{N}-90^\circ\text{N}}$ of $0.3 \text{ Wm}^{-2} \text{ K}^{-1}$.

3.4.2. The AER 1870–2005 Scenario

For the AER scenario the negative forcing is NH-centric (Figure 5a), but the response is global in nature. In the PSST case, the surface energy budget mainly adjusts locally to the TOA forcing and there is little induced atmospheric heat transport between the different regions (Figure 5a), similar to the GHG scenario (Figure 4a). In the VSST case, the largest reduction in temperature occurs in the NH, where the forcing is also highest (Figure 5b). This imbalance between the NH and SH induces an anomalous northward transport of energy out of the SH, in both the atmosphere and the ocean. The impact of heat transport on α_i is well demonstrated in the tropics. The 0°S–30°S tropical region has an estimated time-integrated radiative forcing of -25×10^{22} J (Figure 5a), a positive heat uptake of 15×10^{22} J (Figure 5b), and cools by 0.31 K. By comparison, the NH tropical region has over double the local forcing (-54×10^{22} J; Figure 5a), a negative heat uptake (-22×10^{22} J; Figure 5b), and shows greater cooling (-0.46 K). These local numbers alone would suggest that both regions have similar α_i values to those seen in the GHG case. However, there is also a large atmospheric heat transport of 31×10^{22} J from the 0°S–30°S to the 0°N–30°N region. Accordingly, $\alpha_{0^\circ\text{N}-30^\circ\text{N}}$ ($0.4 \text{ Wm}^{-2} \text{ K}^{-1}$) is much smaller than $\alpha_{0^\circ\text{S}-30^\circ\text{S}}$ ($2.0 \text{ Wm}^{-2} \text{ K}^{-1}$). This smaller value of α in the NH tropics may indicate that the energy transported across the equator into this region fails to have an influence upon surface air temperatures.

Much of this atmospheric energy transported over the equator originates from the 30°S–60°S region, which exhibits a large northward transport of energy (33×10^{22} J) out of the region (Figure 5b). Despite this energy loss, the 30°S–60°S region has both minimal local negative radiative forcing (-7×10^{22} J; Figure 5a) and surface air temperature change (-0.09 K), producing an $\alpha_{30^\circ\text{S}-60^\circ\text{S}}$ of $6.4 \text{ Wm}^{-2} \text{ K}^{-1}$. Thus, CM3 provides a large northward heat transport with minimal surface air temperature change in the 30°S–60°S region. This energy is then released to space in the 0°N–30°N region, where it also has little apparent impact upon surface air temperature. This heat transport leads to the small $\alpha_{0^\circ\text{N}-30^\circ\text{N}}$ being somewhat cancelled out by the larger

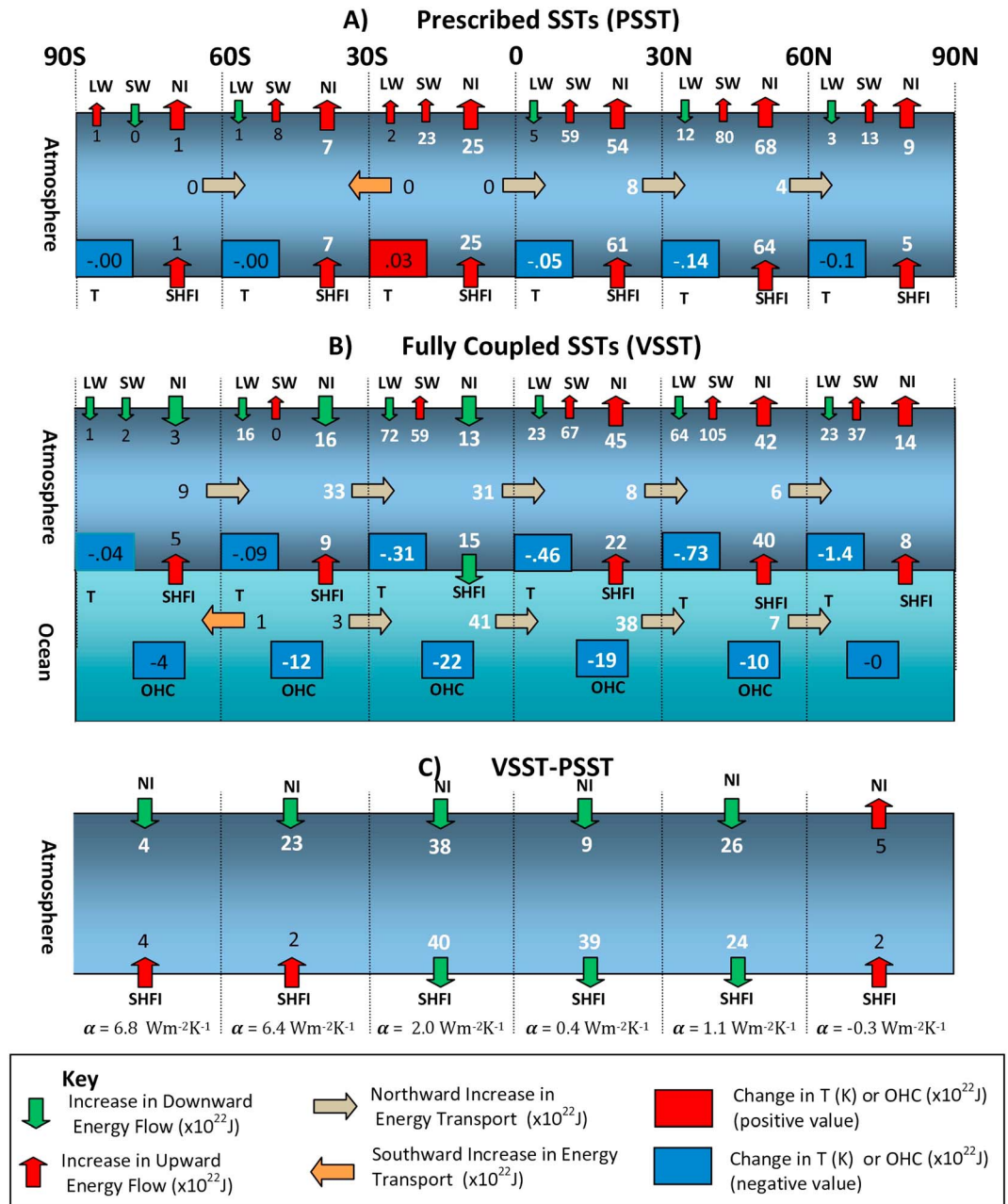


Figure 5. Same as Figure 4 but for the AER experiment.

$\alpha_{30^{\circ}\text{S}-60^{\circ}\text{S}}$, which may explain why, globally, α in the AER case is quite similar to α observed in the GHG case, despite large regional differences in α_i .

While atmospheric heat transport mainly redistributes energy from the SH midlatitudes to the NH tropics, oceanic heat transport redistributes energy from the SH tropics to the NH midlatitude regions. The influence of the oceanic heat transport (Figure 5b) can be seen in the 30°N–60°N region, where the AER scenario forcing (-68×10^{22} J) is strongest and much larger than that of the GHG scenario (35×10^{22} J). However, the magnitude of temperature change in both the GHG and AER cases is almost identical. The $\alpha_{30^{\circ}\text{N}-60^{\circ}\text{N}}$ values are similar for the AER and GHG cases, being 1.1 and $1.0 \text{ Wm}^{-2} \text{ K}^{-1}$, respectively. Therefore, unlike in the NH tropics, the additional energy transported from the SH seems to dampen the temperature response in NH midlatitudes.

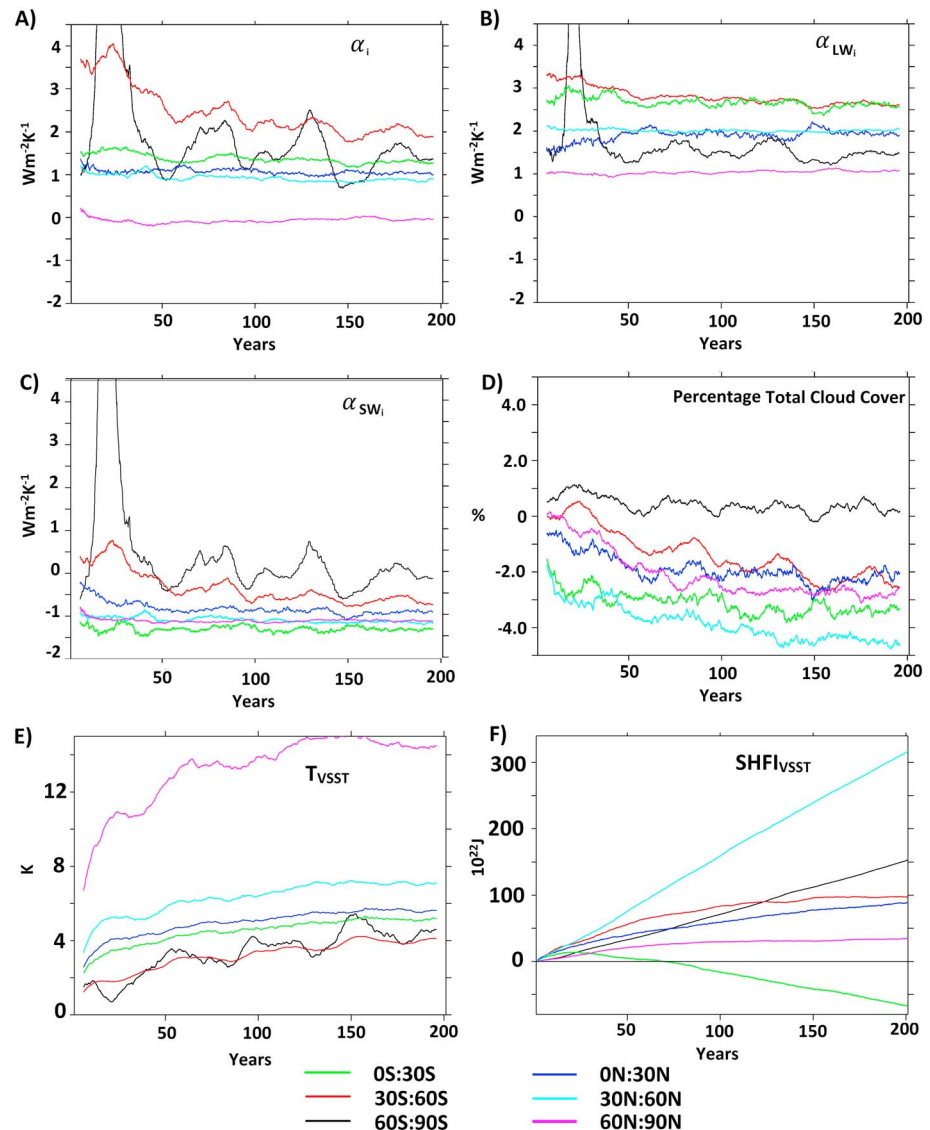


Figure 6. Changes in α_i and its shortwave and longwave components after an instantaneous quadrupling of CO₂. (a) Feedback parameter α_i (the regional climate feedback parameter⁻¹) in Wm⁻²K⁻¹ for the six large-scale regions considered in this work as a function of time after a quadrupling of CO₂ in CM3. (b and c) The longwave and shortwave components of α_i , respectively. (d) The change in percentage total cloud cover in each region after a quadrupling of CO₂. (e) Same as Figure 6d but change in near-surface air temperatures in kelvin. (f) Same as Figure 6d but time-integrated surface heat flux (i.e., SHFI_{VSST}) in units of 10²² J.

3.5. Trends in Regional Climate Feedback Parameters After a Quadrupling of CO₂

After a quadrupling of CO₂, a considerable time dependence was seen in α (Figure 3a) if the PSST forcing was used. This would imply that, in addition to the scenario dependence seen in the local feedback parameters in the AER and GHG cases, there could be a time dependence too. Unfortunately, the unforced variability in the time series of α in the AER and GHG cases is too large (see Figure 2.) for these runs to be used to investigate this. However, using the 10 year average time series of F_{PSST} , N_{VSST} , T_{VSST} , and T_{PSST} to calculate α_i (Figure 6a) from the same quadrupling of CO₂ experiments described in section 3.2 can help us understand which regions may be subject to time dependence in α . (We also performed this analysis using the IE method but show α_i from 10 year average fluxes as it provides better indication of when the value of α_i changes. However, we reach the same conclusions with both methods.)

Figure 6a shows $\alpha_{0^{\circ}S-30^{\circ}S}$, $\alpha_{0^{\circ}N-30^{\circ}N}$ and $\alpha_{30^{\circ}N-60^{\circ}N}$ to be fairly stable over time and with similar values to those seen in the GHG forcing case (i.e., ~ 1 Wm⁻²K⁻¹ in the NH tropics/midlatitudes and ~ 1.4 Wm⁻²K⁻¹

in the SH tropics). Feedback parameter $\alpha_{30^{\circ}\text{S}-60^{\circ}\text{S}}$ shows a considerable negative trend and is larger than in other regions, consistent with findings in both the GHG and AER cases (section 3.3). This result is in contrast to the result of *Armour et al.* [2013] that showed the Community Climate System Model version 4 regional α in the $30^{\circ}\text{S}-60^{\circ}\text{S}$ region to be smaller than in other regions.

To investigate the reason for the high $\alpha_{30^{\circ}\text{S}-60^{\circ}\text{S}}$ values in CM3, we separate out the longwave (LW) and shortwave (SW) components of α_i (Figures 6b and 6c). Figure 6b shows that the LW components of α_i are larger in the $30^{\circ}\text{S}-60^{\circ}\text{S}$ and $0^{\circ}\text{S}-30^{\circ}\text{S}$ regions than elsewhere. For the shortwave component of α_i (Figure 6c), with the exception of regions south of 30°S , most regions have a strong positive feedback (i.e., the shortwave component of α_i is negative), which is in agreement with the GHG case findings (Figure 4). However, there is also a trend in the shortwave component of $\alpha_{30^{\circ}\text{S}-60^{\circ}\text{S}}$ not seen in other regions. The reason that $\alpha_{30^{\circ}\text{S}-60^{\circ}\text{S}}$ is larger than in other regions can therefore be attributed to the lack of positive SW feedback, coupled with a larger LW α_i value, whereas the trend in α_i is predominately due to SW feedback becoming more positive over time.

Senior and Mitchell [2000] and *Williams et al.* [2008] note the importance of changes in cloud cover in causing decadal to centennial changes in α . *Williams et al.* [2008] argue that in certain regions, such as over the Southern Ocean, the lack of initial surface warming leads to a large thermal contrast between the boundary layer and free troposphere. It is this inversion that leads to an increase in cloudiness and therefore a decrease in the TOA imbalance not strongly related to the local surface temperature change (hence a large α_{SW} value in that region). However, as the ocean warms this inversion disappears, and thus, the cloud cover starts to decrease leading to α_{SW} decreasing with time. While we do not see an increase in cloud cover over the Southern Ocean in CM3, we do see a smaller initial decrease in cloud cover after a quadrupling of CO_2 than elsewhere, and this is followed by a more significant decrease over time compared to other regions (Figure 6d, red line versus other colors).

Recently, *Andrews et al.* [2015] have shown that a decrease in α_{SW} is also present in many other Coupled Model Intercomparison Project Phase 5 (CMIP5) models after a quadrupling of CO_2 . Similar to *Williams et al.* [2008] they attribute this to a shift in the regional surface warming pattern. For CMIP5 models they show that in years 1–20 most warming is confined to the Northern Hemisphere and over land, while during years 20–150 there is more warming in the Southern Hemisphere and over ocean.

In Figure 6e for CM3 the change in temperature of each 30° region is plotted following a quadrupling of CO_2 . This demonstrates that CM3 exhibits a shift in warming pattern consistent with other CMIP5 models, with delayed warming in the Southern Hemisphere middle and high latitudes. Our results along with those of *Andrews et al.* [2015], *Senior and Mitchell* [2000], and *Williams et al.* [2008] would seem to indicate that GCMs, like CM3, which do not exhibit much initial warming in the Southern Hemisphere middle-high latitudes compared to other regions, could exhibit a stronger time-varying α that is largely driven by changes in α_{SW} in those regions. However, it is clear that more work is needed to understand what controls the magnitude of the coupling between changes in the regional temperature pattern and α_{SW} .

In most regions the GHG α_i values (Figure 4) are quite near those initially seen after a quadrupling of CO_2 (Figure 6a). In some regions, where α_i shows little or no time dependence, this suggests that idealized experiments can be of use for explaining the historical feedback of the model when forced with the same agents. However, in regions where α_i varies with time, the problem of knowing exactly when in the time series α_i from the idealized experiment is applicable to the historical period remains. More significantly, the values of α_i in the AER case are very different from those observed at any time after a quadrupling of CO_2 . This suggests that values of α_i for the large-scale regions are influenced by the spatial pattern of the radiative forcing and perhaps also the heat transport in the ocean and atmosphere induced by that forcing pattern. Therefore, breaking down the planet into large-scale regions is of little use if one wants to explain the response with constant feedback parameters within these regions.

3.6. Heat Uptake Efficacy

Winton et al. [2010, 2013] introduce the idea of ocean heat uptake efficacy to explain the evolution of α . They postulate that when a positive radiative forcing is applied, the subsequent heat uptake operates akin to a negative radiative forcing. One of their key premises is that negative forcing due to heat uptake produces

a different regional forcing pattern than positive radiative forcing. A second premise is that the forcing pattern is important in determining α . Thus, whenever heat uptake is nonzero, α is a superposition of the pattern brought about by the forcing agent and heat uptake. Accordingly, as the heat uptake pattern changes, and eventually heads to zero during the progression toward equilibrium, α will also change.

Formally defined, heat uptake efficacy (ϵ_N) is the factor by which heat uptake is scaled so that the global temperature decrease brought about by 1 Wm^{-2} heat uptake is equal to that due to 1 Wm^{-2} of CO_2 forcing. The left-hand side of equation (1) is altered to include this scaling, such that

$$\epsilon_N N - F = -\alpha(t_{\text{eq}})T, \quad (8)$$

where $-\alpha(t_{\text{eq}})$ is the climate feedback parameter at a time when the model is in equilibrium, t_{eq} . The question we ask here is whether applying a certain efficacy value allows us to use the F_{PSST} in conjunction with α from the linear extrapolation method. In other words, after a quadrupling of CO_2 can we explain the energy lost from the model progressing from F_{PSST} to F obtained from the linear extrapolation method by heat uptake efficacy? If this were possible it might suggest that α from the linear extrapolation method could be applied to the GHG and AER scenarios if the correct heat uptake efficacy is applied.

We have calculated ϵ_N for the first 180 years after a quadrupling of CO_2 , which is shown in Figure 3c. Here $\alpha(t_{\text{eq}})$ for CM3 is assumed to be $0.75 \text{ Wm}^{-2} \text{ K}^{-1}$ as obtained from the linear extrapolation method, while we use the forcing of 7.6 Wm^{-2} obtained from the F_{PSST} . Figure 3c also shows that a time-varying efficacy is required, and that in order for α to stay constant (as seen in Figure 3a), ϵ_N would need to increase with time from ~ 1.3 to ~ 2.4 . The hope would have been for a constant value, but because the value of efficacy does change, then the problem is shifted from understanding the adjustment in α to understanding the adjustments in efficacy.

A time-varying efficacy implies that the climate feedback parameter due to changes in heat uptake ($-\alpha_N = -\alpha(t_{\text{eq}})/\epsilon_N$) is itself not constant as a function of time. *Rose et al.* [2014] find that slab ocean aqua planets forced with heat uptake in the high latitudes have smaller values of α_N compared those forced with heat uptake in the tropics. In Figure 6f we plot $N|_{\text{VSST}}$ for each 30° region, which demonstrates that CM3 shows a significant shift in heat uptake from low to high latitudes. This would suggest that the reason for time-varying ϵ_N and therefore by definition α could be explained by this shift in heat uptake. This result is not incompatible with the idea presented in section 3.5 that changes in α are tied to the warming pattern of the model [*Andrews et al.*, 2015], as the heat uptake pattern will drive and be driven by changes in the warming pattern. Likewise, the problem is to understand how heat uptake changes couple with α .

3.7. The TCR of CM3

Transient Climate Response (TCR) is defined as the temperature change when a doubling of CO_2 is reached after a 1% rise per year. A recent paper by *Shindell* [2014] estimated an equivalent TCR for aerosols (TCR_{AER}), which they define as

$$\text{TCR}_{\text{AER}} = \frac{F_{2\text{xCO}_2}}{F_{\text{AER}}} T_{\text{AER}}, \quad (9)$$

where $F_{2\text{xCO}_2}$ is the radiative forcing due to a doubling of CO_2 , F_{AER} is the aerosol radiative forcing averaged over 1996–2005, and T_{AER} is the temperature change due to aerosol forcing averaged over 1996–2005.

We define $F_{2\text{xCO}_2}$ as the prescribed SST forcing due to a doubling of CO_2 (3.8 Wm^{-2}) and F_{AER} and F_{GHG} as the prescribed SST forcing from the AER (-1.9 Wm^{-2}) and GHG (3.3 Wm^{-2}) scenarios, respectively, between 1996 and 2005. Likewise, we define the T_{AER} ($-1.0 \pm 0.2 \text{ K}$) and T_{GHG} ($1.7 \pm 0.2 \text{ K}$) as the respective T_{VSST} values averaged between 1996 and 2005. This results in a TCR_{GHG} of $1.9 \pm 0.3 \text{ K}$ and a TCR_{AER} of $2.1 \pm 0.5 \text{ K}$. The similar α values and N_{VSST} (see section 3.1) values we see in response to AER and GHG scenarios means that the closeness of the two results is as expected.

However, *Shindell* [2014] suggests that the CM3 climate is much more sensitive to aerosol (TCR_{AER} of 3.0 K) than to greenhouse gas (TCR_{GHG} of 1.8 K) forcing. *Shindell* [2014] used a similar technique to obtain T_{GHG} (although both $F_{2\text{xCO}_2}$ and F_{GHG} are obtained from linear regression rather than PSST) but defined T_{AER} as the residual of a 1870–2005 CM3 VSST run with all forcing agents (T_{ALL}) included and the sum of two CM3 VSST runs, one with only greenhouse gas forcing (T_{GHG}) and one with natural forcing only (T_{NAT}) included:

$T_{\text{AER}} = T_{\text{ALL}} - (T_{\text{GHG}} + T_{\text{NAT}})$. The ALL and NAT VSST runs of CM3, apart from the different forcing scenarios, are identical to the GHG and AER VSST runs. We calculate TCR using T_{AER} defined from this residual and obtain a value of 2.8 ± 0.5 K, which is much nearer the TCR given by *Shindell* [2014] (the results are not identical due to the different radiative forcing mentioned above and also because *Shindell* [2014] calculates TCR for aerosol and ozone combined).

The origin of this difference between our T_{AER} and that of *Shindell* [2014] for CM3 lies in the fact that the linear addition of the temperature change from individual runs does not match that of a single model run with all of the forcing agents combined. In fact, the sum of T_{NAT} (-0.2 ± 0.2 K), T_{AER} (-1.0 ± 0.2 K), and T_{GHG} (1.7 ± 0.2 K) is 0.3 K greater than T_{ALL} (0.2 ± 0.2 K) calculated from the all forcing model run. This difference of 0.3 K is significant at the 95% level, making natural variability alone an unlikely explanation for the difference. A possible explanation for this nonlinearity may stem from the fact that the all forcing run includes land use changes [*Shindell*, 2014], which is not considered in any of the other runs. At present land use temperature change has not been calculated for CM3. Therefore, further work is needed to understand if differences between our results and those of *Shindell* [2014] are due to a genuine nonlinearity or the result of a combination land use change and unforced variability.

4. Conclusions

The key aim of this paper was to use GFDL CM3 to calculate the global and regional feedback parameters from the energy budgets changes between 1870 and 2005 in response to GHG and AER forcing scenarios. We then ask the simple question of how these values relate to the feedback parameter estimated by the commonly used linear extrapolation method applied to a quadrupling of CO_2 . Our key findings can be summarized as follows:

1. Making use of the IE method (section 2.2) we show a similar α in response to the AER ($1.13 \text{ Wm}^{-2} \text{ K}^{-1}$) and GHG ($1.28 \text{ Wm}^{-2} \text{ K}^{-1}$) scenarios when forced with each agent separately between 1870 and 2005 (section 3.1).
2. These GHG and AER α values are larger than the $0.75 \text{ Wm}^{-2} \text{ K}^{-1}$ estimated using the linear extrapolation method after an instantaneous quadrupling of CO_2 . We demonstrate that this difference is largely due to time dependence in α , which results in the forcing obtained from the GHG and AER PSST runs being incompatible with the α obtained from the linear extrapolation method. This is because the linear extrapolation method includes some of the time dependence in α in the radiative forcing. Hence, we conclude that the α from the linear extrapolation method is not very useful for explaining the 1870–2005 or future temperature change of CM3 if PSST forcing is used. One solution would be to adjust the PSST radiative forcing, but further work is required to understand how this adjustment would vary as a function of both forcing agent and time (section 3.2).
3. The time dependence seen in α_{IE} also implies that for CM3 the energy lost to space does not scale linearly with the average surface temperature change over that time period. Therefore, while calculating the total energy lost to space provides a useful description of the efficiency of the climate system, it is not a particularly useful predictor of future climate change. If the behavior of CM3 is indicative of the real world, this would imply that studies that attempt to estimate future warming based upon past changes in the energy budget could underestimate this warming (section 3.3).
4. Regionally, α_i varied greatly between the GHG and AER scenarios. For example, in the SH midlatitudes and SH tropics, α_i is larger in the AER case, but in the NH tropics it was larger in the GHG case. We conclude that these differences are most likely due to the GHG and AER cases having very different changes in both ocean and atmospheric energy transport (section 3.4).
5. Regionally the α_i values seen in the first 20 years after a quadrupling of CO_2 are similar to those seen in the GHG case. However, we also show that $\alpha_{30^\circ\text{S}-60^\circ\text{S}}$ and $\alpha_{60^\circ\text{S}-90^\circ\text{S}}$ decrease between years 20 and 180. This result seems to disagree with the local climate feedback parameter theory presented by *Armour et al.* [2013] which considers, at a regional level, feedback to be constant. However, similar to both *Rose et al.* [2014] and *Andrews et al.* [2015] we find that much of the time variation in local α_i seems to stem from the shortwave cloud response (section 3.5).
6. We explore the possibility of explaining the time dependence in α using heat uptake efficacy. However, we found that there is a notable time dependence in the efficacy term itself. Therefore, it is unclear which efficacy value from the quadrupling of CO_2 run relates best to the GHG and AER scenarios (section 3.6).

7. Our conclusion of a similar α in response to the GHG and AER cases is in disagreement with *Shindell* [2014]. We show that this difference is likely due to whether the feedback parameter for aerosols is calculated from a separate model run or calculated by the removal of aerosols from the model run with all forcing agents included. This result highlights the possibility of a nonlinear response to the summation of forcing agents in CM3 (section 3.7).

Acknowledgments

We thank C. Golaz and M. Winton for useful discussions and comments. We thank L. Horowitz for performing the model runs used in this paper. We are grateful to the three reviewers for their detailed and helpful comments that greatly aided the preparation of this paper. T.L. Frölicher acknowledges financial support from the SNSF (Ambizione grant PZ00P2_142573). All data from the quadrupling of CO₂ experiments and historical VSST runs are available in CMIP-AR5 archive at http://www.ipcc-data.org/sim/gcm_monthly/AR5/WG1-Archive.html. The remaining historical PSST runs are permanently stored on the GFDL archive file system. This is not accessible to the public, but the data can be made available by the lead author.

References

- Andrews, T. (2009), Forcing and response in simulated 20th and 21st century surface energy and precipitation trends, *J. Geophys. Res.*, *114*, D17110, doi:10.1029/2009JD011749.
- Andrews, T. (2014), Using an AGCM to diagnose historical effective radiative forcing and mechanisms of recent decadal climate change, *J. Clim.*, *27*(3), 1193–1209, doi:10.1175/JCLI-D-13-00336.1.
- Andrews, T., J. M. Gregory, M. J. Webb, and K. E. Taylor (2012), Forcing, feedbacks and climate sensitivity in CMIP5 coupled atmosphere–ocean climate models, *Geophys. Res. Lett.*, *39*, L09712, doi:10.1029/2012GL051607.
- Andrews, T., J. M. Gregory, and M. J. Webb (2015), The dependence of radiative forcing and feedback on evolving patterns of surface temperature change in climate models, *J. Clim.*, *28*(4), 1630–1648, doi:10.1175/JCLI-D-14-00545.1.
- Armour, K. C., C. M. Bitz, and G. H. Roe (2013), Time-varying climate sensitivity from regional feedbacks, *J. Clim.*, *26*(13), 4518–4534, doi:10.1175/JCLI-D-12-00544.1.
- Boucher, O., et al. (2013), 7. Clouds and aerosols, in *Climate Change 2013: The Physical Science Basis. Contribution of Working Group I to the Fifth Assessment Report of the Intergovernmental Panel on Climate Change*, edited by T. F. Stocker et al., pp. 571–657, Cambridge Univ. Press.
- Church, J. A., N. J. White, L. F. Konikow, C. M. Domingues, J. G. Cogley, E. Rignot, J. M. Gregory, M. R. van den Broeke, A. J. Monaghan, and I. Velicogna (2011), Revisiting the Earth's sea-level and energy budgets from 1961 to 2008, *Geophys. Res. Lett.*, *38*, L18601, doi:10.1029/2011GL048794.
- Crook, J. A., P. M. Forster, and N. Stuber (2011), Spatial patterns of modeled climate feedback and contributions to temperature response and polar amplification, *J. Clim.*, *24*(14), 3575–3592, doi:10.1175/2011JCLI3863.1.
- Donner, L. J., et al. (2011), The dynamical core, physical parameterizations, and basic simulation characteristics of the atmospheric component AM3 of the GFDL global coupled model CM3, *J. Clim.*, *24*(13), 3484–3519, doi:10.1175/2011JCLI3955.1.
- Feldl, N., and G. H. Roe (2013), The nonlinear and nonlocal nature of climate feedbacks, *J. Clim.*, *26*(21), 8289–8304, doi:10.1175/JCLI-D-12-00631.1.
- Frölicher, T. L., M. Winton, and J. L. Sarmiento (2014), Continued global warming after CO₂ emissions stoppage, *Nat. Clim. Change*, *4*(1), 40–44, doi:10.1038/nclimate2060.
- Frölicher, T., J. Sarmiento, D. Paynter, J. Dunne, J. P. Krasting, and M. Winton (2015), Dominance of the Southern Ocean in Anthropogenic Carbon and Heat Uptake in CMIP5 Models, *J. Clim.*, *28*(2), 862, doi:10.1175/JCLI-D-14-00117.1.
- Golaz, J.-C., L. W. Horowitz, and H. Levy (2013), Cloud tuning in a coupled climate model: Impact on 20th century warming, *Geophys. Res. Lett.*, *40*, 2246–2251, doi:10.1002/grl.50232.
- Gregory, J., and M. Webb (2008), Tropospheric adjustment induces a cloud component in CO₂ forcing, *J. Clim.*, *21*(1), 58–71, doi:10.1175/2007JCLI1834.1.
- Gregory, J. M., W. J. Ingram, M. A. Palmer, G. S. Jones, P. A. Stott, R. B. Thorpe, J. A. Lowe, T. C. Johns, and K. D. Williams (2004), A new method for diagnosing radiative forcing and climate sensitivity, *Geophys. Res. Lett.*, *31*, L03205, doi:10.1029/2003GL018747.
- Griffies, S. M., et al. (2011), The GFDL CM3 coupled climate model: Characteristics of the ocean and sea ice simulations, *J. Clim.*, *24*(13), 3520–3544, doi:10.1175/2011JCLI3964.1.
- Hansen, J. (2002), Climate forcings in Goddard Institute For Space Studies SI2000 simulations, *J. Geophys. Res.*, *107*(D18), 4347, doi:10.1029/2001JD001143.
- Hansen, J. (2005), Efficacy of climate forcings, *J. Geophys. Res.*, *110*, D18104, doi:10.1029/2005JD005776.
- Kuhlbrodt, T., and J. M. Gregory (2012), Ocean heat uptake and its consequences for the magnitude of sea level rise and climate change, *Geophys. Res. Lett.*, *39*, L18608, doi:10.1029/2012GL052952.
- Kummer, J. R., and A. E. Dessler (2014), The impact of forcing efficacy on the equilibrium climate sensitivity, *Geophys. Res. Lett.*, *41*, 3565–3568, doi:10.1002/2014GL060046.
- Levy, H., L. W. Horowitz, M. D. Schwarzkopf, Y. Ming, J.-C. Golaz, V. Naik, and V. Ramaswamy (2013), The roles of aerosol direct and indirect effects in past and future climate change, *J. Geophys. Res. Atmos.*, *118*, 4521–4532, doi:10.1002/jgrd.50192.
- Lewis, N., and J. A. Curry (2014), The implications for climate sensitivity of AR5 forcing and heat uptake estimates, *Clim. Dyn.*, doi:10.1007/s00382-014-2342-y.
- Li, C., J.-S. Storch, and J. Marotzke (2012), Deep-ocean heat uptake and equilibrium climate response, *Clim. Dyn.*, *40*(5–6), 1071–1086, doi:10.1007/s00382-012-1350-z.
- Ming, Y., V. Ramaswamy, L. J. Donner, and V. T. J. Phillips (2006), A new parameterization of cloud droplet activation applicable to general, *J. Atmos. Sci.*, *63*(4), 1348–1356.
- Murphy, D. M., S. Solomon, R. W. Portmann, K. H. Rosenlof, P. M. Forster, and T. Wong (2009), An observationally based energy balance for the Earth since 1950, *J. Geophys. Res.*, *114*, D17107, doi:10.1029/2009JD012105.
- Murphy, J. M. (1995), Transient response of the Hadley Centre coupled ocean–atmosphere model to increasing carbon dioxide. Part III: Analysis of global-mean response using simple models, *J. Clim.*, *8*, 496–514.
- Myhre, G., et al. (2013), 2013: Anthropogenic and natural radiative forcing, in *Climate Change 2013: The Physical Science Basis. Contribution of Working Group I to the Fifth Assessment Report of the Intergovernmental Panel on Climate Change*, edited by T. F. Stocker et al., pp. 659–740, Cambridge Univ. Press, Cambridge, U. K., and New York.
- Otto, A., et al. (2013), Energy budget constraints on climate response, *Nat. Geosci.*, *6*(6), 415–416, doi:10.1038/ngeo1836.
- Rayner, N. A., D. E. Parker, E. B. Horton, C. K. Folland, L. V. Alexander, D. P. Rowell, E. C. Kent, and A. Kaplan (2003), Global analyses of sea surface temperature, sea ice, and night marine air temperature since the late nineteenth century, *J. Geophys. Res.*, *108*(D14), 4407, doi:10.1029/2002JD002670.
- Rose, B. E. J., K. C. Armour, D. S. Battisti, N. Feldl, and D. D. B. Koll (2014), The dependence of transient climate sensitivity and radiative feedbacks on the spatial pattern of ocean heat uptake, *Geophys. Res. Lett.*, *41*, 1071–1078, doi:10.1002/2013GL058955.
- Schwarzkopf, M. D., and V. Ramaswamy (1999), Radiative effects of CH₄, N₂O, halocarbons and the foreign-broadened H₂O continuum: A GCM experiment, *J. Geophys. Res.*, *104*, 9467–9488, doi:10.1029/1999JD900003.

- Senior, A., and J. Mitchell (2000), The time-dependence of climate sensitivity, *Geophys. Res. Lett.*, *27*(17), 2685–2688, doi:10.1029/2000GL011373.
- Shindell, D. T. (2014), Inhomogeneous forcing and transient climate sensitivity, *Nat. Clim. Change*, *4*(4), 18–21, doi:10.1038/NCLIMATE2136.
- Shine, K. P. (2003), An alternative to radiative forcing for estimating the relative importance of climate change mechanisms, *Geophys. Res. Lett.*, *30*(20, 2047), doi:10.1029/2003GL018141.
- Williams, K. D., W. J. Ingram, and J. M. Gregory (2008), Time variation of effective climate sensitivity in GCMs, *J. Clim.*, *21*(19), 5076–5090, doi:10.1175/2008JCLI2371.1.
- Winton, M., K. Takahashi, and I. M. Held (2010), Importance of ocean heat uptake efficacy to transient climate change, *J. Clim.*, *23*(9), 2333–2344, doi:10.1175/2009JCLI3139.1.
- Winton, M., A. Adcroft, S. M. Griffies, R. W. Hallberg, L. W. Horowitz, and R. J. Stouffer (2013), Influence of ocean and atmosphere components on simulated climate sensitivities, *J. Clim.*, *26*(1), 231–245, doi:10.1175/JCLI-D-12-00121.1.